



Published in final edited form as:

Nat Neurosci. 2010 March ; 13(3): 361–368. doi:10.1038/nn.2490.

Dichotomy of functional organization in the mouse auditory cortex

Sharba Bandyopadhyay^{1,2}, Shihab A. Shamma^{2,3}, and Patrick O. Kanold^{1,2,†}

¹Department of Biology, University of Maryland, College Park

²Institute for Systems Research, University of Maryland, College Park

³Department for Electrical and Computer Engineering, University of Maryland, College Park

Abstract

The sensory areas of the cerebral cortex possess multiple topographic representations of sensory dimensions. Gradient of frequency selectivity (tonotopy) is the dominant organizational feature in the primary auditory cortex, while other feature-based organizations are less well established. We probed the topographic organization of the mouse auditory cortex at the single cell level using *in vivo* two-photon Ca²⁺ imaging. Tonotopy was present on a large scale but was fractured on a fine scale. Intensity tuning, important in level-invariant representation, was observed in individual cells but was not topographically organized. The presence or near-absence of putative sub-threshold responses revealed a dichotomy in topographic organization. Inclusion of sub-threshold responses revealed a topographic clustering of neurons with similar response properties, while such clustering was absent in supra-threshold responses. This dichotomy indicates that groups of nearby neurons with locally shared inputs can perform independent parallel computations in ACX.

Neurons in sensory cortical areas are organized into vertical columns^{1, 2} such that neurons with similar stimulus selectivity are clustered together. Columns, in turn, are arranged in maps so that columns with similar response properties are nearby^{1–3}.

Encoding of stimuli in the primary auditory cortex (A1) is thought to be sparse^{4, 5}, with a multitude of overlaid maps representing different stimulus dimensions^{3, 6}. The dominant topographic feature in the auditory cortex (ACX) is a tonotopic map, which is best seen at moderate to near-threshold sound levels^{7–9}. Different ACX regions can be distinguished based on the direction of the frequency gradient or its expression^{3, 6, 9}. Other forms of patchy organization overlaying the tonotopic map have been described. These include organizations based on the bandwidth of frequency integration, tuning to intensity, selectivity or suppression of binaural inputs, selectivity for the direction and speed of frequency modulation, and the periodicity of the stimulus^{3, 6}. Such maps were revealed

Users may view, print, copy, download and text and data- mine the content in such documents, for the purposes of academic research, subject always to the full Conditions of use: http://www.nature.com/authors/editorial_policies/license.html#terms

[†]Corresponding author: Patrick O. Kanold, Dept. of Biology, University of Maryland, 1116 Biosciences Res. Bldg, College Park, MD 20742, USA, Phone: +1 (301) 405.5741, pkanold@umd.edu.

Author contributions: SB performed *in vivo* studies. SB and POK performed *in vitro* studies. POK planned and supervised the project. SB, SAS, and POK contributed to experimental design, discussed the results and wrote the manuscript.

using techniques with limited spatial resolution, such as single unit recording (100–200 μm) 3, 6–10, intrinsic imaging ($> 200 \mu\text{m}$) 11, 12, and voltage sensitive dyes ($> 200 \mu\text{m}$) 13, 14. Thus the fine scale architecture of ACX remains unknown.

Here, we overcome these limitations by using in vivo two-photon imaging of functional responses in mouse ACX using Ca^{2+} sensitive dyes 15–17. This allows imaging of the functional microarchitecture of cortical maps with single cell resolution. To probe for the existence of “maps” of response properties we take advantage of the ability to image the activity of many neurons simultaneously, and develop general methods for identifying maps.

Results

We bulk-loaded mouse ACX (**Fig. 1a–d**) with the Ca^{2+} indicators Fluo-4 AM (P18–P35, $n = 24$) or OGB-1 AM (P13–P32, $n = 15$) (**Fig. 1d**) using visually guided pressure injection. Increases in Ca^{2+} were observed in response to both sinusoidally amplitude modulated (SAM) tones and broadband noise sounds (**Fig. 1e**). Both brief and sustained fluorescence increases (**Fig. 1e**) were observed. In any given neuron, tone evoked responses were often maximal at a specific frequency (defined as the neurons’ preferred, or characteristic frequency, CF, as in **Fig. 3a**). Some neurons responded monotonically with increasing stimulus intensity. Others were nonmonotonic with intensity, achieving a maximal response at an intermediate (“best”) intensity and then decreasing beyond that as shown in **Fig. 6** and **Fig. 7**, (see Methods for precise definition of these response measures). However, even at their CF or best intensity, neurons did not always respond to every presentation of the stimulus (**Fig. 2b**, S2). Thus, mean Ca^{2+} increases were lower (2–7%) than single trial responses ($\sim 10\%$ dF/F , Fig. 1e, Fig. 2b, Fig. S2). While OGB-1 and Fluo-4 responses were similar the signal-to-noise ratio was lower with OGB-1 18–20. The disparity in mean fluorescence and single trial fluorescence was quantified as reliability or fraction of responsive trials (see Methods for definition). The mean reliability to a set of stimuli varied from 0.02–0.5 with Fluo-4 (Fig. 2c) and 0.02–1 with OGB-1 and was higher with OGB-1 (median 0.28 $n = 15$) than Fluo-4 (median 0.18, $n = 24$, $P < 10^{-10}$, ranksum) (Fig. 2c). Since these were mean values over a set of stimuli, some stimuli (like at CF or best intensity) produced higher reliability. For example, broadband noise stimuli typically (if monotonic) resulted in increased reliability with increasing stimulus intensity (Fig. 2b). However, as reported previously, a fraction of neurons in the imaged field did not respond to any presented auditory stimulus (Fig. 2d) 5, 21. While median responsiveness was similar for the 2 dyes (OGB-1: 75%, Fluo-4: 66%, $P = 0.11$, ranksum, Fig. 2d) the distributions were different ($P = 0.011$ One sided 2-sample KS test). The median maximum response strengths with OGB-1 and Fluo-4 was 3% (Fig. 2e) which corresponds to only a few spikes (< 10 spikes/s, based on our in vitro recordings, see Fig. 8e,f and Fig. S4), consistent with relatively low firing rates⁵ in the auditory cortex to tones or broadband noise.

Tonotopy present in coarse but not in fine spatial scales

Previous microelectrode studies showed multiple different functional areas within the mouse ACX²². These areas are defined by distinct frequency tuning properties and gradients of the tonotopic map²². All such maps (by definition) in any species were primarily delineated

based on responses to tones and other simple stimuli^{3, 6}. While ACX neurons have been additionally characterized by their responses to vocalizations, natural sounds and other complex stimuli^{23–29}, systematic mapping studies have not been done with such stimuli. Thus to describe the basic topographic organization of the mouse auditory cortical areas, and to lay the ground for future more elaborate characterizations we focused on the simpler stimuli used previously^{3, 6}. By imaging different areas along the cortical surface we identified multiple areas of ACX based on their tuned responses to tones and direction of gradient of the CF at moderate sound levels (40–60 dB SPL) (Fig. 3 and Fig. 4) ($n = 9$, Fluo-4).

A1 neurons had strong responses to tones, usually with single-peaked tuning curves^{9, 22} (Fig. 3a, b, cells 4–8). An area containing such neurons is illustrated in Fig. 3c. Imaged areas in A1 clearly showed a coarse progression of CF from lower (~ 16 kHz, blue) to higher (~ 32 kHz, brown) frequencies (Fig. 3c and d). In addition to a part of A1, parts of two other ACX regions could be identified in this animal: the ultra frequency (UF), and the dorsal posterior (DP) region. Both UF and DP lacked clear progression of CFs and were characterized by weak responses to tones and very broad or multi-peaked tuning curves^{9, 22} (Fig. 3b, cells 1–3). While neurons in the UF region were generally tuned to very high frequencies (> 45 kHz), they were sometimes also responsive to lower frequencies as shown in Fig. 3b (cells 1–3). The general location of the imaging site with respect to different functional regions of the mouse ACX²² is depicted in Fig. 3e (white dashed rectangular region) based on the responses in different fields. The imaged location in A1 was confirmed to be thalamo-recipient using retrograde labeling of thalamic projections (Fig. 3f). Figure 4 illustrates the differences in CF progression in A1 (Fig. 4a) and the anterior auditory field (AAF; Fig. 4b) regions of ACX imaged in two other animals. AAF exhibited a progression of CFs although with high variability from lower (~ 10 kHz, blue) to higher (~ 23 kHz, green) frequencies in a direction (rostral to caudal) opposite to that seen in A1 (caudal to rostral, Fig. 4a inset) (Fig. 4c). These results, therefore, confirm the existence of several fields of mouse ACX with coarsely differentiated single cell responses²², and in particular, coarse tonotopic gradients in both A1 and AAF (Fig. 4c).

Previous studies of A1 analyzed tonotopy on a large spatial scale level (> 100 μm)^{3, 6}. We also observed this general progression of frequency selectivity in A1 and AAF (~ 1 octave/350 μm , median 2.7 octaves/mm in A1 and -2.3 octaves mm^{-1} in AAF, $n = 9$ animals, Fig. 4c) in the rostro-caudal dimension. However, when examined closely we found a great degree of overlap of surrounding frequencies (often more than an octave apart) that locally degraded the tonotopic map (Fig. 4a, b). Furthermore, the population distribution of CF variability within a field of view was large (Fig. 4d). We used d' analysis (Fig. 4e) to calculate the distance needed to reliably detect different tonotopic regions. With such a large variability, we calculated that the CF difference needed to discriminate A1 regions is $1/0.85 = 1.2$ octaves (0.85 from Fig. 4d). Given the median slope (2.7 octaves mm^{-1}) two locations within ~ 400 μm cannot be distinguished.

Lack of organized bandwidth maps

While a tonotopic axis is present in A1 of all species examined thus far, it is unknown what stimulus features are mapped in the orthogonal direction, the isofrequency axis. Single unit recordings in various species indicated a patchy organization along this axis based on such response properties as intensity tuning and bandwidth 3, 6. In contrast, imaging showed that sharply and broadly tuned neurons could be right next to each other (Fig. 5a and b) showing a lack of fine organization based on tuning curve bandwidths.

Quantification of the heterogeneity by calculating the bandwidth variability showed it to be large, especially with Fluo-4 compared to OGB-1 (Fig. 5c). Thus, based on the fine scale mapping with two-photon imaging in the mouse A1, the representation of frequency tuning and across-frequency integration is far more heterogeneous than previously seen with single unit recordings and intrinsic imaging in several species, including the mouse.

Lack of organized intensity maps

Given the absence of fine scale organization based on iso-intensity frequency tuning, we next probed the organization for intensity tuning. ACX neurons are responsive to broadband stimuli, such as broadband noise. Mean responses to broadband noise stimuli of increasing intensity were monotonic in some neurons and nonmonotonic in others (Fig. 6a and Fig. 7a).

Nonmonotonic coding of sound intensity can be utilized in level-invariant representation of sound objects 30 and it has been proposed from single unit recordings that organized patchy maps of intensity tuning exist 3, 6, 31. We used broadband stimuli to probe for the existence of clusters or maps based on preferred intensity. Broadband noise is useful for this purpose as in a given imaged area there were neurons of varying CFs (see Fig. 3 and 4). The responsiveness of each neuron within an imaging field as a function of intensity is reflected in activation plots such as those of Figs. 6b and S3. Patches of cells were activated best together at different intensities, but the numbers of neurons activated varied nonmonotonically with intensity (Fig. 6c and S3). Furthermore, individual neurons that respond to different intensities were spatially intermingled (Fig. 6d) as can be seen in the heterogeneous mix of response properties of the neuronal population when accumulating data from different intensity combinations (e.g., 3 levels in Fig. 6d and Fig. S3C, colored squares). This local heterogeneity was confirmed by imaging multiple areas of ACX and reconstructing the intensity preferences of individual neurons (Fig. 7). It was then quantified by calculating the variability of the best intensity in the imaged area on a cell-by-cell basis. This analysis showed that there was a large variability of best intensities (Fig. 7b, less with OGB-1 than with Fluo-4) across ACX. For an organized intensity map to exist there should be a gradient of best intensity across the medio-lateral (iso-frequency) axis A1. Given the range of 70 dB (based on our data) of preferred noise intensity variation and a medio-lateral extent of 0.7 mm of A1 22 a predicted slope of best intensity would be 100 dB mm^{-1} . We investigated the existence of such a slope by analyzing the variability of best intensity distribution of our imaging sites. Based on the median variability of best intensity (Fig. 7b) d' analysis shows that to reliably detect differences in best intensity one would have to be $\sim 300 \mu\text{m}$ apart resulting in a detected intensity difference of 33 dB. Given the medio-lateral extent of our imaging sites ($< 300 \mu\text{m}$, Fig. 7a), our data do not provide any evidence for

such a gradient and thus for an organized intensity map. An alternative organization to a best intensity gradient is the existence of microdomains of neurons with similar best intensity. To identify such microdomains of potentially patchy intensity selectivity we quantified the average number of neurons in a local neighborhood of each neuron (5 nearest neighbors) with the same intensity preference as the central neuron. Cumulative distribution of average percentage of neighboring neurons with the same preferred intensity (Fig. 7c) shows a high degree of heterogeneity (more with Fluo-4 than with OGB-1) suggesting that while some clusters of neurons with similar intensity preferences do exist, they represent only a fraction of all neurons in ACX.

Dichotomy in spatial organization of neurons with different response properties

The response selectivity of neurons is typically calculated based on the maximum of the response (dF/F) mean during the stimulation period (for example 17, 32, 33, Fig. 3). This response measure is related to total number of spikes in the response³⁴ and thus our analysis is equivalent to those based on average firing rate. However, this analysis ignores differences in spike timing, which can also convey different information about the stimulus^{35, 36} and might be spatially organized. The entire Ca^{2+} trace (although at a coarse temporal resolution) has information about both spike time, spike rate and possibly some subthreshold membrane voltage fluctuations that depend on the affinity of dye used.

We developed a general method (see Methods) to identify response similarity maps based on the entire significant portion of the Ca^{2+} (dF/F) waveform during stimulation and also in the period following stimulation (off-period, Fig. 1e, Fig. S1C). Neurons with similar response waveforms were grouped together based on k -means clustering of the significant principal components of the response waveforms to a set of intensities of broadband noise or to a set of tone frequencies. The number of clusters was varied between 2 and 15 (average 2 cells per cluster see Methods) until a preset criterion of cluster tightness was met. When the preset criterion was not met within 15 clusters we set the number of clusters to 15, which signified no significant clustering.

The center of the cluster (the centroid) represents the mean response of cells within a cluster to a particular stimulus set and thus contains information about both the stimulus selectivity and temporal response pattern. Figure 8a shows four cluster centroids obtained with responses to SAM noise at different intensities. The four different response patterns (4 colors) show distinct response classes (monotonic and weak, blue and 1; non-monotonic with different preferred intensities or time delay to response peak, other 3 clusters). Using OGB-1 as the Ca^{2+} indicator we often ($\sim 50\%$ $n = 154/290$ sets) found significant spatially clustered groups of cells with clear sharp transitions between response classes within a field of view (Fig. 8b; lower right image shows the location of cells belonging to clusters described by centroids in Fig. 8a). This indicates that cells within this field of view showed similar response waveforms to the same set of stimuli. By contrast, such spatial segregation was considerably less common (Z -value 7.931, Z -test for proportions) using Fluo-4 as the Ca^{2+} indicator ($\sim 20\%$ $n = 70/321$, Fig. 8b). The number of clusters formed was generally larger with Fluo-4 than with OGB-1 (Fig. 8c; $P < 10^{-6}$, KS-test) while there were similar number of cells per imaging site with OGB-1 (38) and Fluo-4 (34) ($P = 0.45$, ranksum).

Further, there were fewer cells per cluster with Fluo-4 than with OGB-1 ($p < 10^{-5}$ one sided KS-test; Fig. 8c). To characterize spatial local heterogeneity of responses we quantified the number of cells in the local neighborhood (5 nearest neighbors) of a single cell that belonged to the same cluster as the central cell (Fig. 8d). The fraction was higher with OGB-1 than with Fluo-4 (median of 40% with OGB-1 versus 20% for Fluo-4. $P < 10^{-6}$, ranksum). Thus cells were more similar to the neighbors with OGB-1 than Fluo-4 (Fig. 8d). Thus with Fluo-4 there is more local heterogeneity than with OGB-1. These results show a clear dichotomy in spatial arrangement of neuronal response properties seen with the 2 dyes.

Since the Ca^{2+} affinities of OGB-1 ($K_d = 170$ nM) and Fluo-4 ($K_d = 350$ nM) are different these dyes might detect a different fraction of a putative subthreshold response. We tested the ability of the two dyes to detect subthreshold depolarizations directly by recordings in vitro in brain slices (Fig. 8e-g). Current (I_m) was injected to evoke a depolarization just below spike threshold (Fig. 8e left, $< \Theta$) or above spike threshold (Fig. 8e, right, $> \Theta$). Below spike threshold only OGB-1 showed dF/F changes (Fig. 8e, g, $P < 0.001$). However, when cells spiked both Fluo-4 and OGB-1 showed dF/F changes and those changes were larger with Fluo-4 (Fig. 8e). Thus as expected 37, responses with Fluo-4 are biased towards suprathreshold responses with no detectable contribution from subthreshold membrane voltage changes (Fig. 8e, f). In contrast as expected from the higher affinity values 19, 20, Ca^{2+} responses with the higher affinity dye OGB-1 can detect subthreshold membrane voltage changes (Figs. 8e, f). Since subthreshold depolarizations are generated by excitatory input, we verified directly that synaptic stimulation could lead to detectable Ca^{2+} responses (Fig. 8g and S4). Electrical stimulation of synaptic inputs causes EPSPs and significant mean Ca^{2+} fluorescence signals with OGB-1 (Fig. 8g) while not with Fluo-4 (see Fig. S5). Thus, together these data suggest that OGB-1 can detect subthreshold and suprathreshold activity, while Fluo-4 only detects suprathreshold responses 37.

We observed a higher mean reliability in vivo in responses seen with OGB-1 (median 0.28) compared to Fluo-4 (median 0.18, $P < 10^{-10}$ ranksum) (Fig. 2c). Since spiking responses to a given depolarization can have failures, the enhanced reliability of OGB-1 suggests detection of a larger fraction of sub-threshold activity in vivo with OGB-1. Further, the variability in CF shows a trend for lower variability with OGB-1 than Fluo-4 (although not significant, Fig. 4d) and variability in preferred intensity and bandwidth (Fig. 7b and Fig. 5c respectively) in the population was significantly lower with OGB-1 than with Fluo-4. These differences can also be accounted for by the fact that OGB-1 detects subthreshold responses while Fluo-4 does not. Thus, using these two different dyes allowed us to differentially probe for organization based on predominantly supra-threshold (Fluo-4) or combined supra-threshold and sub-threshold responses (OGB-1).

Given that OGB-1 reports a larger fraction of sub-threshold activity than Fluo-4 (Fig. 8e-g), this suggests that nearby ACX neurons have high degree of shared inputs. The lack of spatial segregation and highly spatially inhomogeneous responses with Fluo-4 suggests heterogeneity of supra-threshold responses. Since Fluo-4 responses reflect primarily suprathreshold activity this suggests that neurons perform independent computations on these shared inputs (Fig. S6).

Discussion

A key finding in our study is the presence of diverse frequency selectivity and best intensity in neurons in close proximity (as close as 20 μm). This suggests the lack of organization of precise maps based on frequency selectivity, frequency integration, or intensity selectivity. In contrast, we reveal a fine scale organization in ACX when using dyes (OGB-1) that reflect subthreshold Ca^{2+} changes in addition to those dependent on spiking. These maps are likely derived from shared inputs to a population of neurons. Studies in the visual cortex using OGB-117, 32, 33 use stimuli such as oriented bars that evoke responses with large number of spikes unlike the low response rates in the ACX obtained with tone and noise stimuli⁵. Thus it is unlikely that in the studies of visual cortex small (1%, Fig. S4) sub-threshold fluctuations were seen with large Ca^{2+} responses (up to 30%¹⁷) caused by high spike rates.

The presence of maps based on the temporal responses of neurons has not been reported before and suggests that inputs to ACX cells are spatially organized. The absence of such clustered organization with dyes that primarily reflect spiking activity (Fluo-4) suggests very heterogeneous processing of inputs by nearby neurons from largely shared inputs. Since cortical columns can have highly specific fine-scale embedded networks^{38–40}, they could generate heterogeneous and spatially intermingled responses. In addition, the presence of a population of neurons with diverse response properties but with shared input selectivity might imply the existence of multiple parallel ascending pathways in ACX. In addition these results also indicate that there is little neuronal redundancy in each “column” as each neuron seems to have a unique set of stimulus selectivity and response properties.

Previous studies of ACX used techniques that have spatial resolution of 100–200 μm showed that frequency selectivity and intensity tuning vary systematically across the cortical surface^{3, 6, 31}. The lack of a clear organization based on frequency selectivity and intensity tuning here might be due to some key technical differences. In contrast to a coarse sampling of neurons by repeated penetrations with a single electrode, 2-photon imaging reports cell activity with single cell resolution of all loaded neurons in an area. Thus, 2-photon imaging removes biases in cell selection²¹ and crosstalk from nearby neurons.

Moreover, neuronal responses are modulated by the type and depth of anesthesia, and hence that can alter the observed organization. Early studies in unanesthetized cats had indicated weak tonotopy and a lack of organization based on spectral integration bandwidth in A141–43. Similarly, studies in awake primate A1 indicated a lack of clear organization based on spectral integration bandwidth and intensity preference⁴⁴. Both of these results are similar to our study in the isoflurane (0.5–1%) anesthetized mouse. In contrast, studies showing the presence of tight tonotopy and an organization based on spectral integration and best intensity were mostly done in deeply barbiturate (or ketamine) anaesthetized cats, rodents, and primates^{3, 6, 10}. Thus, while (gross) tonotopy is present in all conditions, its precision and the presence of other organizational features might depend on the specific anesthetic state of the animal. Since the suppression of neuronal processing by anesthesia depends on its type and depth⁴⁵, anesthesia in varying degrees could selectively highlight organization present due to shared inputs (Fig. 8). Alternatively, the lack of intensity and bandwidth maps

in our study could reflect species differences as for example orientation maps are present in cat but absent in rodent visual cortex¹⁷. In addition, our data is obtained from cells primarily in layer II/III. It is possible that, response maps could have a different organization in layer IV^{44, 46}.

The heterogeneity of frequency selectivity, intensity tuning, and bandwidth in ACX does not exclude the presence of precise maps based on other stimulus features or other more complex stimuli. Two-photon imaging offers a general fine-grained unbiased approach to discovering such maps based on response properties that can also be applied to other areas of the brain. Furthermore, when coupled with the observed dichotomy of absence and presence of maps based on primarily supra-threshold or combined supra- and sub-threshold responses, our findings indicate a possibly general feature of cortical processing in that local neurons receive shared inputs but perform independent computations.

Methods Summary

Animal Preparation

Mice (C57BL6J) aged P13 – P35 were anesthetized using 2–3% isoflurane in oxygen. A small craniotomy (~ 2 mm diameter) was made over auditory cortex (see below). The intact exposed dura was covered with saline. A hollow tube was attached to the cut contralateral ear canal for sound delivery. For imaging, isoflurane anesthesia was reduced to 0.5–1% while maintaining an areflexive state of the animal with animal skin temperature usually at ~ 33–35°C. All procedures were approved by the University of Maryland IACUC.

Confirmation of imaging location in A1

The location of the craniotomy was determined stereotactically (70% of bregma-lambda and ~2 mm ventral or ~ 4.4 mm lateral). Our dye injection site was guided by vasculature²² (Figure S1A). Following imaging we inserted DiI crystals into the imaging site with a 26 gauge needle. Brain was stored in 4% paraformaldehyde at 38°C, for > 3 weeks and slices (100–200 μm) were cut to confirm labeling in the medial geniculate body (MGB) (Figure S1B). We also confirmed the imaging location by injecting anterograde tracers (cholera toxin-B) into the MGB stereotactically. After 3 days, following a craniotomy in the imaging location the presence of terminals of MGB projections in layer 3 and 4 (Fig. 1a–c) was verified. Following imaging of terminals slices were cut to confirm tracer injection in the MGB (Fig. 1a). Finally we confirmed cell responses in A1–AAF based on latency of the response. Our single unit recordings (Fig. S1C) in awake mouse A1 show latencies of ~ 20 ms. While imaging at ~ 200 ms resolution one cannot detect this latency in single cells, by analyzing the time course of responses in the stimulus onset frame we detected the onset peak of neuropil responses ~ 30 ms into the frame (Fig. S1D). Thus, cells in our imaging location had similar latencies as A1 cells.

Auditory Stimulation

Sound stimuli were digitally generated using custom software written in Matlab (Mathworks) and generated by a DA board (National Instruments), anti alias filtered (PD-AAF-18. United Electronics, Inc.), attenuated (TDT PA5), and delivered (TDT EC1) via a

hollow coupler tube. The sound system was calibrated over a range of 6–70 kHz and showed a smooth spectrum (± 10 dB). Overall sound pressure level on average was ~ 80 dB SPL (for tones). No correction (equalization) was done to compensate for the changes in the acoustic calibration. Most ambient noise due to the laser was below 5 kHz. Since mice have very high hearing thresholds below 5 kHz²², this noise did not affect our experiments. Acoustic stimuli were SAM (5 Hz, modulation depth of 1) tones at different frequencies or SAM noise (usually 8–64 kHz bandwidth) of different loudness since AM stimuli elicit stronger responses²⁷ compared to non-AM stimuli. Occasionally tone or noise pip trains (100–150 ms duration at intervals of 200–300 ms) were used. Each stimulus was repeated 6–15 times at 0.1–0.25 Hz.

Two-photon calcium imaging

AM calcium dye (Oregon Green 488 BAPTA-1 (OGB-1) or Fluo-4, Invitrogen) was prepared by dissolving 50 μg of dye in 4 μl of 20% pluronic acid in DMSO (Invitrogen) and diluted (1:5–8) with ACSF15, 17 containing either 100 μM AlexaFluor 594 (for visualization) or SR-101 (for visualization and astrocyte identification). Pipettes (2–4 μm tip diameter) were pulled (Sutter P2000), filled with the dye solution and introduced into the cortex. The pipette tip was visualized under two-photon scanning mode and gradually advanced. Dye was pressure injected at a depth of 350–500 μm with 5–20 psi (PV830 Pneumatic PicoPump, WPI) pressure pulses (0.2 to 1 s, 50–130 pulses total over 15 min). Once loaded cells (30–60 min post injection) were observed the pipette was withdrawn and craniotomy was covered with warm agarose and cover-slipped. Imaging was done using a two-photon laser-scanning microscope (Ultima IV, Prairie Technologies) with a Spectra Physics Mai Tai Deep See Ti-Sapphire mode-locked femto-second laser. Excitation wavelength was 800 or 810 nm for OGB1 and Fluo-4, and 870 nm for SR-101. Cells were imaged using a 20 \times or 40 \times water immersion objective (LUMPlanFI/IR Olympus 0.95 or 0.8NA) at depths of usually 150–350 μm from the cortical surface. In 2-photon experiments *z*-sectioning increases the SNR, unlike in epifluorescent Ca^{2+} -measurements, where the signal is contaminated by out-of-focus fluorescence. Images were acquired simultaneously in 2 channels using a 570 nm dichroic filter. Full frame images were acquired at a resolution of 256 \times 256 pixels at 4–10 Hz. Sequences (15–30 frames) were acquired for each stimulus (onset usually at the 10th frame, duration of 5–10 frames). Cells were considered to have a significant response if the 95% confidence interval of the mean dF/F value in at least one of the frames during stimulus presentation did not encompass zero (baseline). In some experiments to acquire data at faster rates we performed linescans (50–100 Hz) by drawing lines, freehand, along which the laser scanned. Scanning was repeated usually 1000 times (~ 10 –20 ms each line). Analysis of dF/F was performed as in frame scans (Fig. S2).

Sulforhodamine (SR-101) as indicator for astrocytes

SR-101 has been used as a specific marker for astrocytes^{32, 47} and we often found selective uptake of SR-101 by morphologically astrocyte like cells. However in a number of experiments we found SR-101 to be taken up by other cells possibly neurons, especially after 2–3 hours following dye loading. Neurons might take up SR-101 based on activity or possibly through gap junctions⁴⁸. Since our observations did not indicate selective uptake of

SR101 by astrocytes we could not reliably separate neuron from glia as has been reported previously¹².

Negative fluorescence changes

We observed negative fluorescence changes with some stimuli in response to stimulation (on-period) or in the period following stimulus presentation (off-period) with either OGB-1 or Fluo-4. This might reflect inhibition in the Ca^{2+} signal^{33, 49}. As the fluorescence trace includes sub-threshold activity (less with Fluo-4 than OGB, Fig. 8e-g) along with inhibitory responses and information about spiking we used the clustering approach of the entire fluorescence waveform (see below) as a measure of the response to stimulus to obtain a more general depiction of the activity than detecting spikes only or estimating firing rates from the fluorescence signal as done previously^{37, 49}.

Two-photon image analysis

Images were analyzed using custom software written in Matlab (Mathworks). Cells were visualized using the average image of all frames. Cells were marked with a circle of 2 or 3 pixels radius, which usually encompassed the soma. Base line fluorescence was estimated from 3-6 frames preceding stimulus onset, as an average from the multiple stimulus repeats. Mean fluorescence of each cell was estimated for all the frames and then converted into dF/F . Bootstrap mean dF/F values are used for all calculations. 95% confidence intervals of estimates of mean dF/F were obtained using bootstrap resampling. For some of the data we employed motion correction. For X - Y plane movements we used a correlation-based correction with translation in X - Y over 5-10 pixels. If the pixel-by-pixel correlation increased significantly from the correlation at the (0,0) location the image was shifted accordingly. Such shifts did not happen often and did not cause significant changes in CF or best intensity of cells. With lack of signal improvement and this correction being time intensive it was not routinely performed. For Z movements we performed averaging over 8-15 trials to eliminate noise introduced by such fluctuations when present. Correction based on dF/F values obtained from the red ($> 570\text{nm}$) channel did not cause changes in CF and best intensity and hence was not performed routinely. In particular such correction is not ideal as it assumes dF/F changes in the red channel are due to Z movements exclusively, which is not true due to leakage of dye signal into the red channel.

Reliability Analysis

Mean reliability to a set of stimuli (either a set of SAM tones of different frequencies or a set of SAM broadband noise of different intensities) was calculated from responses to those stimuli in the set to which there was a significant mean response based on 95% confidence intervals. When there was a significant response in the mean, single trial responses were analyzed by thresholding the Ca^{2+} signal at 1.96 of the standard deviation of each frame. The number of trials in which the dF/F crossed threshold at least once in the stimulation frames were considered as responsive trials, and based on that reliability was calculated as the fraction of responsive trials. The mean of that for each cell over a set of stimuli was calculated and used in the distribution of Fig. 2c.

Response Measures

Best intensity was defined as the intensity at which the maximum of mean response (dF/F) was the highest. If this intensity was not the highest intensity used we checked if there was at least one higher intensity at which the response was significantly lower, otherwise the highest intensity was defined as the best intensity. CF for each cell was defined as the frequency producing the largest significant dF/F . Bandwidth of tuning curves was determined as the frequency extent at half-maximum response strength. Extrapolation or symmetry assumption was used for cases at the boundary.

Cluster analysis

To investigate local correlations of responses and detect classes of neurons with similar response properties with spatial segregation clustering on the Ca^{2+} responses was performed. A set of responses of cells in a field of view (either responses to noise at different intensities or to 3 tones spaced $1/4^{\text{th}}$ octaves apart at fixed intensity) the dF/F values at every frame during the stimulus and the frames following the end of the stimulus were appended together to form a single response vector r_i , $i = \text{cell number}$. A response matrix $R = [r_1 r_2 \dots r_i \dots r_N]$, of all the cells ($N = \text{total number of cells}$) was created. Principal components analysis was performed on the matrix to obtain a reduced representation (number of components were such that the 99.5% energy was retained). Following this k-means clustering was performed on the principal component projections. k of k-means was varied from 2–15 and the clustering was stopped when the ratio of the mean intra-cluster Euclidean distances and the mean inter-cluster distances was less than 1. The corresponding k was used as the number of clusters. Tighter clusters with the criterion set to 0.5 did not change result of the differences between OGB-1 and Fluo-4. Absence of clustering was indicated if the criterion was not reached by $k = 15$. Maximum k (15) was chosen as median number of cells in the field of view was ~ 35 , and $k = 15$ corresponds to average 2 cells per cluster following which clusters would have 1 cell indicating lack of clustering.

In vitro recording

Slice physiology methods are as published previously 50. Mice are deeply anesthetized with isoflurane (Halocarbon). A block of brain containing ACX was removed and slices (350–400 μm thick) were cut on a vibrating microtome (Leica) in ice-cold ACSF containing (in mM): 130 NaCl, 3 KCl, 1.25 KH_2PO_4 , 20 NaHCO_3 , 10 glucose, 1.3 MgSO_4 , 2.5 CaCl_2 (pH 7.35–7.4, in 95% O_2 –5% CO_2), incubated for 1 hour in ACSF at 30C and then at room temperature. For recording, slices were held in a chamber under the 2-photon microscope and superfused (2–4 ml/min) with ACSF at room temperature. Electrodes were filled with (in mM) 110 K-gluconate, 4 KCl, 4 NaCl, 0.2 CaCl_2 , 10 HEPES, 2 Mg-ATP, 1 MgCl_2 and 5 glutathione (pH 7.2, 300 mOsm). 40 μM OGB-1 or Fluo-4 (K-salt, Invitrogen) was added to the pipette solution at the day of the experiment. Whole-cell recordings were performed with a patch clamp amplifier (Multiclamp 700B, Axon Instruments). Data were acquired with an AD board (National Instruments) using custom software written in MATLAB (Mathworks). Electrical stimulation was applied with a stimulus isolator (Cygnus). Stimuli were applied every 30s and responses to 10–20 repeats were averaged. Sequences of images were

acquired during whole cell recordings at ~ 10 Hz, similar to in vivo experiments. Imaging frame duration, dwell times and analysis were similar to in vivo experiments.

Supplementary Material

Refer to Web version on PubMed Central for supplementary material.

Acknowledgements

Supported by NIDCD R21 DC009454 (POK), NIDCD R01DC009607 (POK), R01DC005779 (SAS), AFOSR DURIP (SAS & POK), and ISR Seed Grant (SAS & POK). The authors also thank D. Winkowski for many helpful comments and help with imaging and J. Zemskova and A. Sheikh for histological help.

References

1. Mountcastle VB. The columnar organization of the neocortex. *Brain*. 1997; 120(Pt 4):701–722. [PubMed: 9153131]
2. Hubel DH, Wiesel TN. Ferrier lecture. Functional architecture of macaque monkey visual cortex. *Proc R Soc Lond B Biol Sci*. 1977; 198:1–59. [PubMed: 20635]
3. Schreiner CE, Winer JA. Auditory cortex mapmaking: principles, projections, and plasticity. *Neuron*. 2007; 56:356–365. [PubMed: 17964251]
4. Koulakov AA, Hromadka T, Zador AM. Correlated connectivity and the distribution of firing rates in the neocortex. *J Neurosci*. 2009; 29:3685–3694. [PubMed: 19321765]
5. Hromadka T, Deweese MR, Zador AM. Sparse representation of sounds in the unanesthetized auditory cortex. *PLoS Biol*. 2008; 6:e16. [PubMed: 18232737]
6. Schreiner CE, Read HL, Sutter ML. Modular organization of frequency integration in primary auditory cortex. *Annu Rev Neurosci*. 2000; 23:501–529. [PubMed: 10845073]
7. Bizley JK, Nodal FR, Nelken I, King AJ. Functional Organization of Ferret Auditory Cortex. *Cereb Cortex*. 2005
8. Merzenich MM, Knight PL, Roth GL. Cochleotopic organization of primary auditory cortex in the cat. *Brain Res*. 1973; 63:343–346. [PubMed: 4764302]
9. Ehret G. The auditory cortex. *J Comp Physiol [A]*. 1997; 181:547–557.
10. Recanzone GH, Schreiner CE, Sutter ML, Beitel RE, Merzenich MM. Functional organization of spectral receptive fields in the primary auditory cortex of the owl monkey. *J Comp Neurol*. 1999; 415:460–481. [PubMed: 10570456]
11. Nelken I, et al. Large-scale organization of ferret auditory cortex revealed using continuous acquisition of intrinsic optical signals. *J Neurophysiol*. 2004; 92:2574–2588. [PubMed: 15152018]
12. Kalatsky VA, Polley DB, Merzenich MM, Schreiner CE, Stryker MP. Fine functional organization of auditory cortex revealed by Fourier optical imaging. *Proc Natl Acad Sci U S A*. 2005; 102:13325–13330. [PubMed: 16141342]
13. Blasdel GG, Salama G. Voltage-sensitive dyes reveal a modular organization in monkey striate cortex. *Nature*. 1986; 321:579–585. [PubMed: 3713842]
14. Tsytsarev V, Fukuyama H, Pope D, Pumbo E, Kimura M. Optical imaging of interaural time difference representation in rat auditory cortex. *Front Neuroengineering*. 2009; 2:2.
15. Stosiek C, Garaschuk O, Holthoff K, Konnerth A. In vivo two-photon calcium imaging of neuronal networks. *Proc Natl Acad Sci U S A*. 2003; 100:7319–7324. [PubMed: 12777621]
16. Svoboda K, Yasuda R. Principles of two-photon excitation microscopy and its applications to neuroscience. *Neuron*. 2006; 50:823–839. [PubMed: 16772166]
17. Ohki K, Chung S, Ch'ng YH, Kara P, Reid RC. Functional imaging with cellular resolution reveals precise micro-architecture in visual cortex. *Nature*. 2005; 433:597–603. [PubMed: 15660108]
18. Yasuda R, et al. Imaging calcium concentration dynamics in small neuronal compartments. *Sci STKE*. 2004; 2004:15.

19. Thomas D, et al. A comparison of fluorescent Ca²⁺ indicator properties and their use in measuring elementary and global Ca²⁺ signals. *Cell Calcium*. 2000; 28:213–223. [PubMed: 11032777]
20. Paredes RM, Etzler JC, Watts LT, Zheng W, Lechleiter JD. Chemical calcium indicators. *Methods*. 2008; 46:143–151. [PubMed: 18929663]
21. Shoham S, O'Connor DH, Segev R. How silent is the brain: is there a "dark matter" problem in neuroscience? *J Comp Physiol A Neuroethol Sens Neural Behav Physiol*. 2006; 192:777–784. [PubMed: 16550391]
22. Stiebler I, Neulist R, Fichtel I, Ehret G. The auditory cortex of the house mouse: left-right differences, tonotopic organization and quantitative analysis of frequency representation. *J Comp Physiol [A]*. 1997; 181:559–571.
23. Wang X, Kadia SC. Differential representation of species-specific primate vocalizations in the auditory cortices of marmoset and cat. *J Neurophysiol*. 2001; 86:2616–2620. [PubMed: 11698547]
24. Galindo-Leon EE, Lin FG, Liu RC. Inhibitory plasticity in a lateral band improves cortical detection of natural vocalizations. *Neuron*. 2009; 62:705–716. [PubMed: 19524529]
25. Barbour DL, Wang X. Contrast tuning in auditory cortex. *Science*. 2003; 299:1073–1075. [PubMed: 12586943]
26. Kowalski N, Depireux DA, Shamma SA. Analysis of dynamic spectra in ferret primary auditory cortex. I. Characteristics of single-unit responses to moving ripple spectra. *J Neurophysiol*. 1996; 76:3503–3523. [PubMed: 8930289]
27. Wang X, Lu T, Snider RK, Liang L. Sustained firing in auditory cortex evoked by preferred stimuli. *Nature*. 2005; 435:341–346. [PubMed: 15902257]
28. deCharms RC, Blake DT, Merzenich MM. Optimizing sound features for cortical neurons. *Science*. 1998; 280:1439–1443. [PubMed: 9603734]
29. Nelken I, Rotman Y, Bar Yosef O. Responses of auditory-cortex neurons to structural features of natural sounds. *Nature*. 1999; 397:154–157. [PubMed: 9923676]
30. Sadagopan S, Wang X. Level invariant representation of sounds by populations of neurons in primary auditory cortex. *J Neurosci*. 2008; 28:3415–3426. [PubMed: 18367608]
31. Polley DB, Read HL, Storace DA, Merzenich MM. Multiparametric auditory receptive field organization across five cortical fields in the albino rat. *J Neurophysiol*. 2007; 97:3621–3638. [PubMed: 17376842]
32. Schummers J, Yu H, Sur M. Tuned responses of astrocytes and their influence on hemodynamic signals in the visual cortex. *Science*. 2008; 320:1638–1643. [PubMed: 18566287]
33. Li Y, Van Hooser SD, Mazurek M, White LE, Fitzpatrick D. Experience with moving visual stimuli drives the early development of cortical direction selectivity. *Nature*. 2008; 456:952–956. [PubMed: 18946471]
34. Smetters D, Majewska A, Yuste R. Detecting action potentials in neuronal populations with calcium imaging. *Methods*. 1999; 18:215–221. [PubMed: 10356353]
35. Young ED, Sachs MB. Representation of steady-state vowels in the temporal aspects of the discharge patterns of populations of auditory-nerve fibers. *J Acoust Soc Am*. 1979; 66:1381–1403. [PubMed: 500976]
36. Bandyopadhyay S, Young ED. Discrimination of voiced stop consonants based on auditory nerve discharges. *J Neurosci*. 2004; 24:531–541. [PubMed: 14724253]
37. Sato TR, Gray NW, Mainen ZF, Svoboda K. The Functional Microarchitecture of the Mouse Barrel Cortex. *PLoS Biol*. 2007; 5:e189. [PubMed: 17622195]
38. Song S, Sjöström PJ, Reigl M, Nelson S, Chklovskii DB. Highly nonrandom features of synaptic connectivity in local cortical circuits. *PLoS Biol*. 2005; 3:e68. [PubMed: 15737062]
39. Yoshimura Y, Dantzker JL, Callaway EM. Excitatory cortical neurons form fine-scale functional networks. *Nature*. 2005; 433:868–873. [PubMed: 15729343]
40. Yoshimura Y, Callaway EM. Fine-scale specificity of cortical networks depends on inhibitory cell type and connectivity. *Nat Neurosci*. 2005; 8:1552–1559. [PubMed: 16222228]
41. Evans EF, Ross HF, Whitfield IC. The spatial distribution of unit characteristic frequency in the primary auditory cortex of the cat. *J Physiol*. 1965; 179:238–247. [PubMed: 5853890]

42. Goldstein MH Jr, Abeles M. Note on tonotopic organization of primary auditory cortex in the cat. *Brain Res.* 1975; 100:188–191. [PubMed: 1182512]
43. Goldstein MH Jr, Abeles M, Daly RL, McIntosh J. Functional architecture in cat primary auditory cortex: tonotopic organization. *J Neurophysiol.* 1970; 33:188–197. [PubMed: 5411513]
44. Recanzone GH, Guard DC, Phan ML. Frequency and intensity response properties of single neurons in the auditory cortex of the behaving macaque monkey. *J Neurophysiol.* 2000; 83:2315–2331. [PubMed: 10758136]
45. Christiaan Stronks H, Aarts MC, Klis SF. Effects of isoflurane on auditory evoked potentials in the cochlea and brainstem of guinea pigs. *Hear Res.* 2009
46. Wallace MN, Palmer AR. Laminar differences in the response properties of cells in the primary auditory cortex. *Exp Brain Res.* 2008; 184:179–191. [PubMed: 17828392]
47. Nimmerjahn A, Kirchhoff F, Kerr JN, Helmchen F. Sulforhodamine 101 as a specific marker of astroglia in the neocortex in vivo. *Nat Methods.* 2004; 1:31–37. [PubMed: 15782150]
48. Keifer J, Vyas D, Houk JC. Sulforhodamine labeling of neural circuits engaged in motor pattern generation in the in vitro turtle brainstem-cerebellum. *J Neurosci.* 1992; 12:3187–3199. [PubMed: 1494952]
49. Moreaux L, Laurent G. A simple method to reconstruct firing rates from dendritic calcium signals. *Front Neurosci.* 2008; 2:176–185. [PubMed: 19225590]
50. Zhao C, Kao JPY, Kanold PO. Functional Excitatory Microcircuits in Neonatal Cortex Connect Thalamus and Layer 4. *Journal of Neuroscience.* 2009; 29:15479–11488. [PubMed: 20007472]

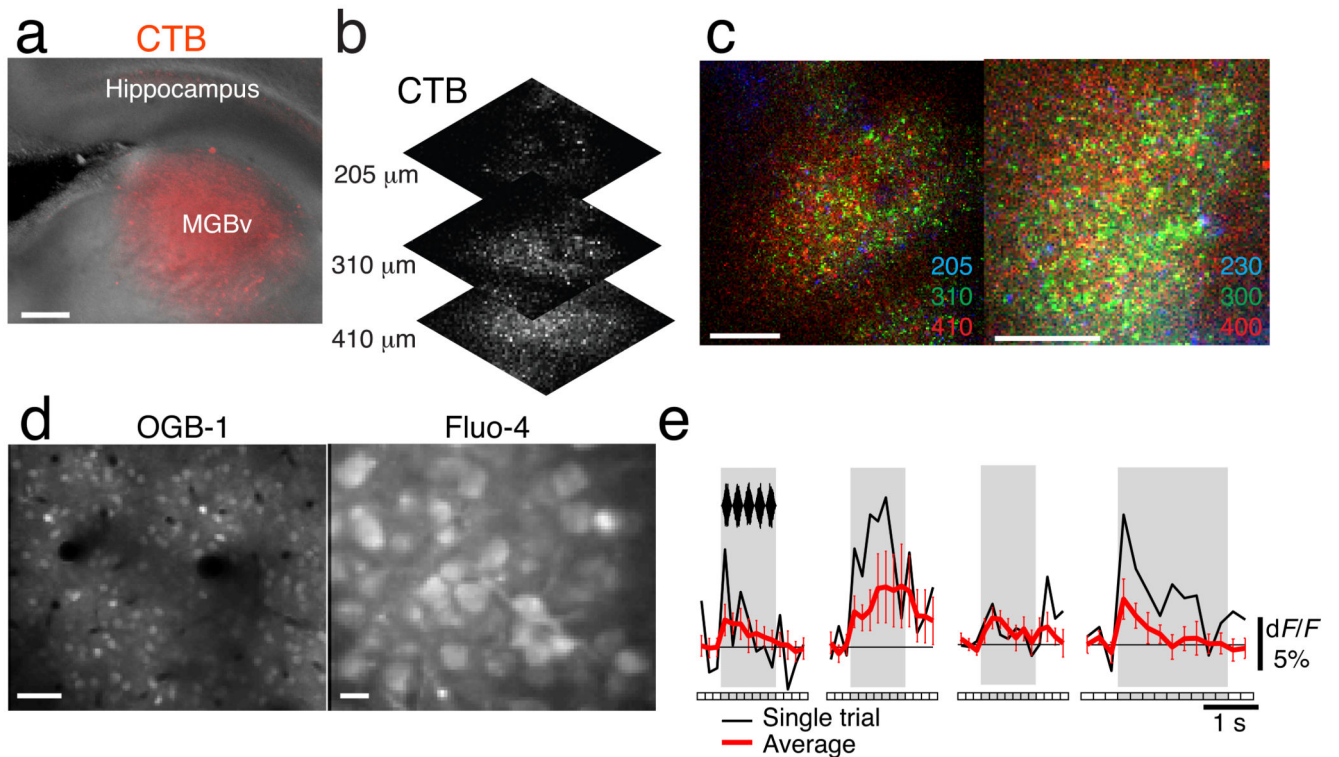


Figure 1. Functional 2-photon Ca^{2+} imaging in mouse ACX

a–c: Confirmation of craniotomy and imaging site in ACX by anterograde labeling.

Cholera toxin-B was injected into the MGB stereotactically (**a**). A craniotomy was performed at our imaging locations. Fluorescently labeled terminals were imaged at 3 depths of 205, 310 and 410 μm from the cortical surface (**b**). Following imaging of terminals *in vivo* slices were cut to confirm tracer injection in the MGB (**a**). **c:** Superposition of images taken at different depths in 2 animals are shown. Note that most signals originated at 300–400 μm depth indicating the thalamo-recipient layer. Thus our imaging location is in A1. Scale bars in **a** and **c**: 100 μm . **d:** Shown are images of bulk loading ACX with OGB-1 (left) and Fluo-4 (right). The area over which cells were loaded varied in experiments from 200 μm to 1 mm diameter regions. Scale bars are 50 μm (left) and 10 μm (right) **e:** Shown are single trial (black) and mean (red) fluorescence changes (dF/F) with SAM broadband noise from 4 different cells. Error bars show 95% confidence intervals indicating a significant fluorescence change. Frame timing is shown below fluorescence trace.

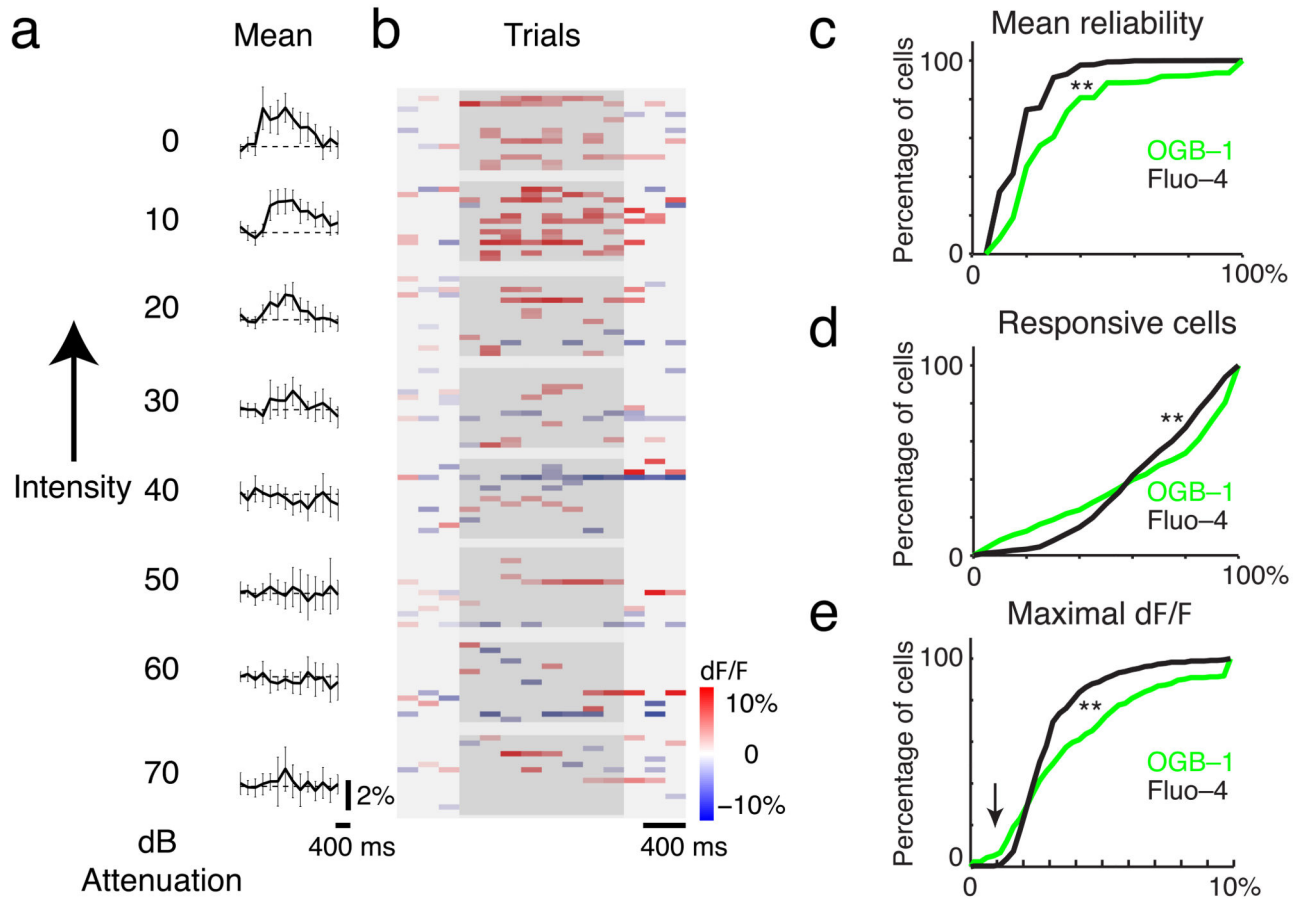


Figure 2. ACX Ca^{2+} responses are unreliable

a: Traces show mean fluorescence changes (dF/F) in one cell for SAM noise of varying intensity. Significant responses at 0–30 dB attenuations were seen in this case. Errorbars show 95% confidence intervals. **b:** Thresholded fluorescence changes (dF/F) (colorbar to right) in all individual trials for the same cell. Gray backgrounds depict stimulation period. Note the unreliability but larger dF/F of single trials. **c:** Cumulative distribution of mean reliability in all imaged cells with Fluo-4 (black) and OGB-1 (green). Mean reliability was defined as the fraction of trials with significant responses (methods) in each cell for a set of stimuli (either different intensities of SAM noise or different frequencies of SAM tone or noise or tone pips). **d:** Cumulative distribution of the fraction of responsive cells in each imaged field (same animals as in **c**). A responsive cell was defined as a cell that responded at least to one of the presented stimuli significantly (95% confidence interval). **e:** Cumulative distribution of maximum response in each field. Mean maximum response is higher with OGB-1 (4.8%) than Fluo-4 (3.3%, $p < 0.05$, t-test, same animals as in **c** and **d**).

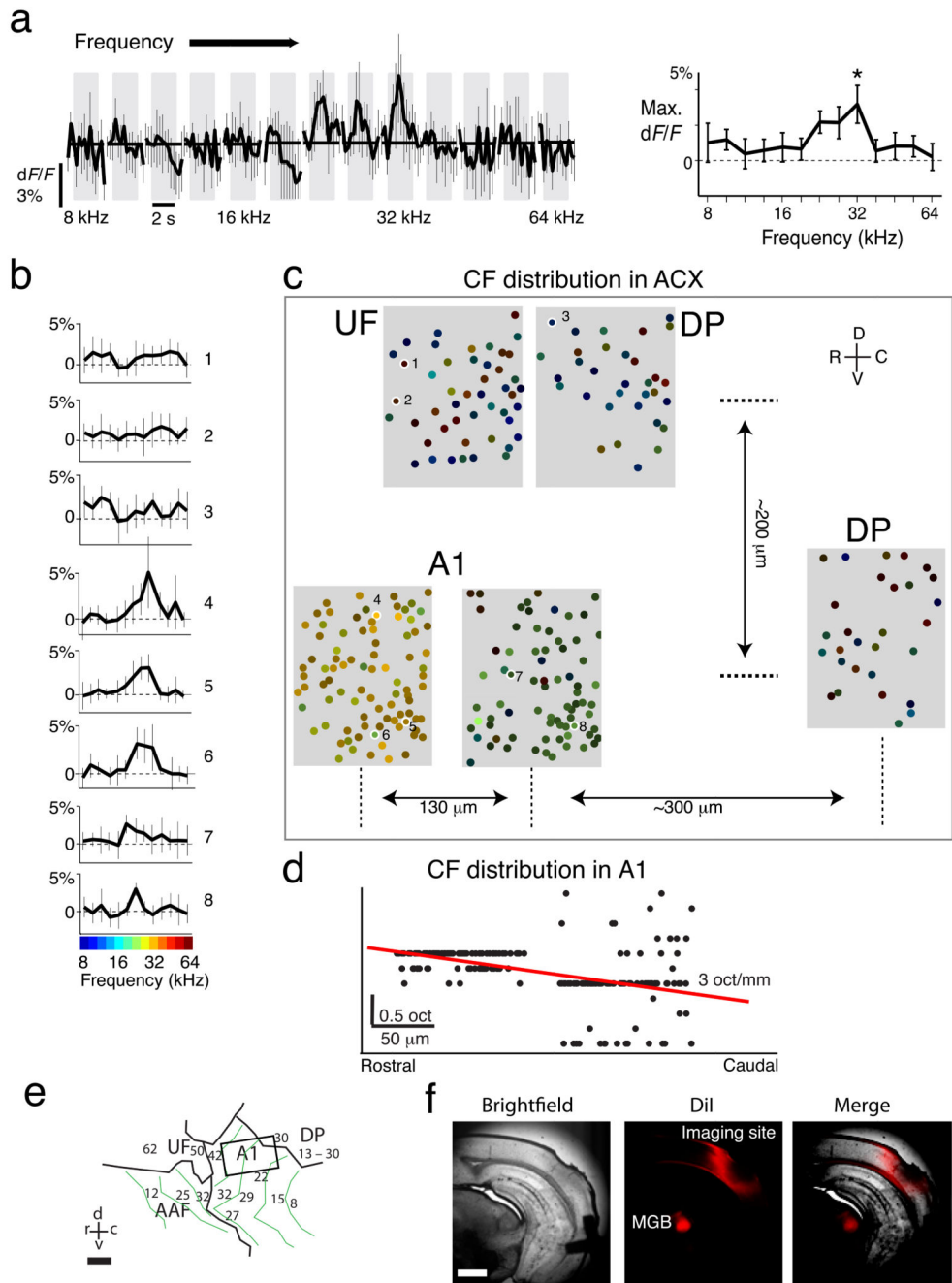


Figure 3. Large scale organization of ACX probed with single cell resolution

a: Traces show responses (dF/F) of single neurons in A1 to SAM tones of various stimulus frequencies (duration indicated by gray area). Plotted is the mean response with 95% confidence intervals. Right: Plotting peak dF/F versus stimulation frequency (tuning curve) shows unimodal tuning (CF = 32 kHz, '*'). **b:** Tuning curves from 8 cells imaged in one animal (locations indicated in **c**). CF progresses from cell 4 to 8. **c:** Reconstructions of the large-scale organization of ACX in one animal by imaging multiple sites. The relative distances (approximate) between centers of imaged sites (gray boxes) are indicated. Relative

positions not to scale. Color denotes CF (colorbar in **b**) based on peak dF/F and luminance response strength. E.g. cells tuned to 38 kHz are orange. Strongly responding cells are bright orange, while weakly responding cells are dark orange. Different regions of ACX are identified based on CF and tuning curve shape (**b**): A1, DP and UF. **d**: Progression of cell CF as a function of rostro-caudal position. Red line indicates best fit. **e**: Large-scale organization of mouse ACX redrawn from 22. Box indicates putative location of imaging site in A1 (**c**). Because of inter-animal variation 22 exact positions of UF and DP relative to A1 in **c** are slightly different. This is a rough depiction as clear demarcations of the different regions are lacking. Scale bar = 250 μm . **f**: Post-hoc verification of A1 imaging site (**c**) by DiI injection. MGB is retrogradely labeled. Damage on imaging site is from DiI crystal insertion after imaging. Scale bar = 1 mm.

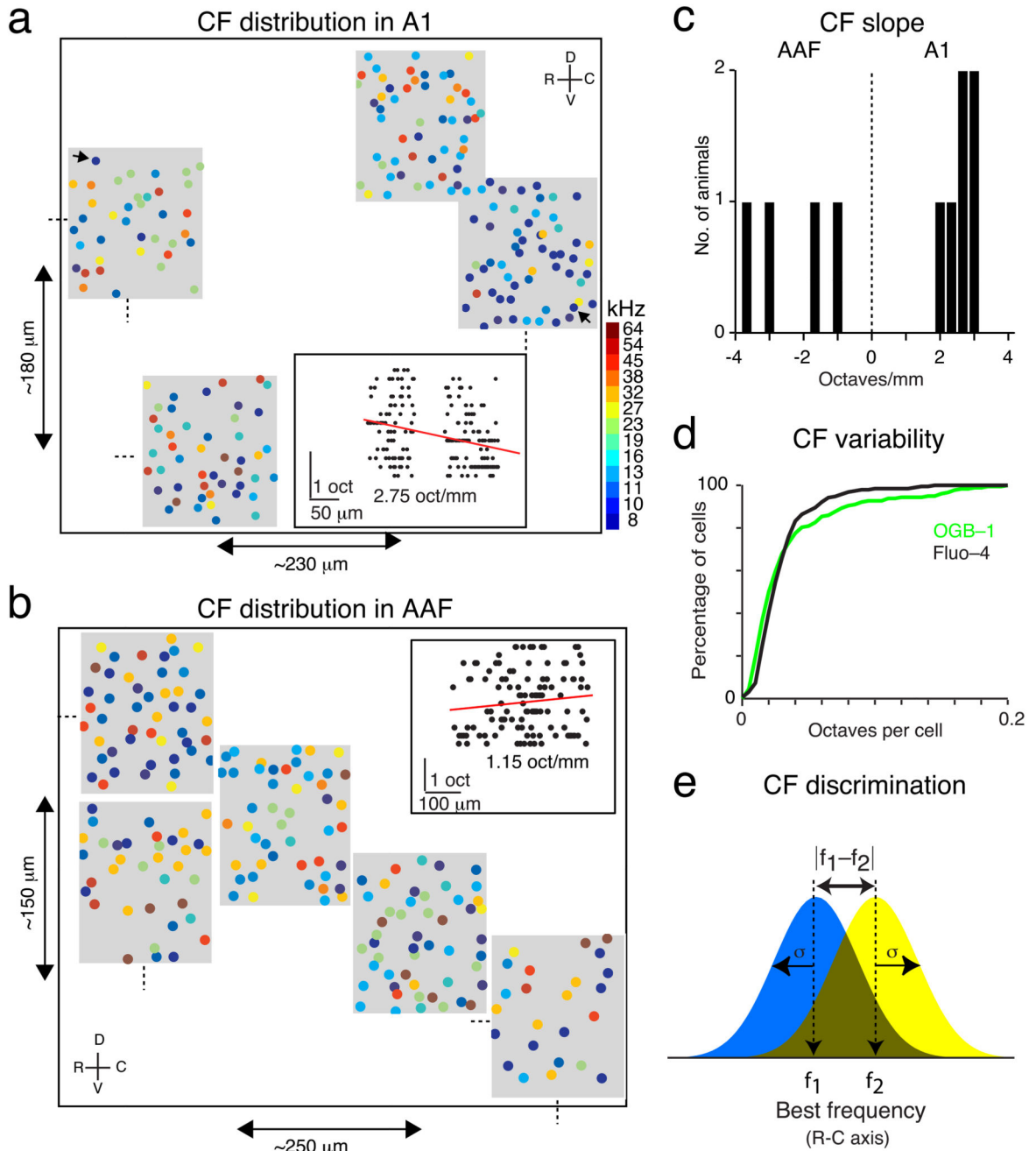


Figure 4. Tonotopy exists in A1 and AAF on large but not on small spatial scales

a: Reconstruction of 4 imaging sites (relative positions are approximate) in A1 in one animal. Cell CF is indicated by color and increases from caudal (~ 10 kHz) to rostral (~ 23 kHz). Cells at opposite A1 ends can show similar CF's (arrows). Positive CF gradient (inset) indicates that imaging site was in A1. **b:** Reconstruction of 5 imaging sites (relative positions are approximate) in ACX in one animal (different from **a**). Negative CF gradient (maximum slope after rotation and exclusion of neurons that were in secondary region, inset) indicates that imaging site was in AAF. **c:** Slope of CF gradient in rostro-caudal

direction from fits to CFs and their respective cells' location (see **a**, **b**, and **Fig. 3d**). Due to inter animal variability and slight differences in animal position, the CF gradient that was fit could occur at an angle from the rostro-caudal axis. Positive or negative CF slopes characterize A1 or AAF respectively. Since not the entire extent of ACX was covered in each animal CF slopes are an estimate of the large-scale CF progression. **d**: Cumulative distribution of CF variability (standard deviation of CF normalized by number of cells in imaged field) within ACX. Variability (median 0.025 octaves/cell, 34 cells per site, average 0.85 octaves per $\sim 100\mu\text{m}^2$) was similar for OGB-1 and Fluo-4 ($P > 0.1$; OGB-1 $n = 15$; Fluo-4 $n = 24$ animals). **e**: d' analysis of sharpness of tonotopy. d' is the mean CF difference at different A1 locations normalized by the standard deviation. $d' = 1$ indicates that mean CFs can be discriminated.

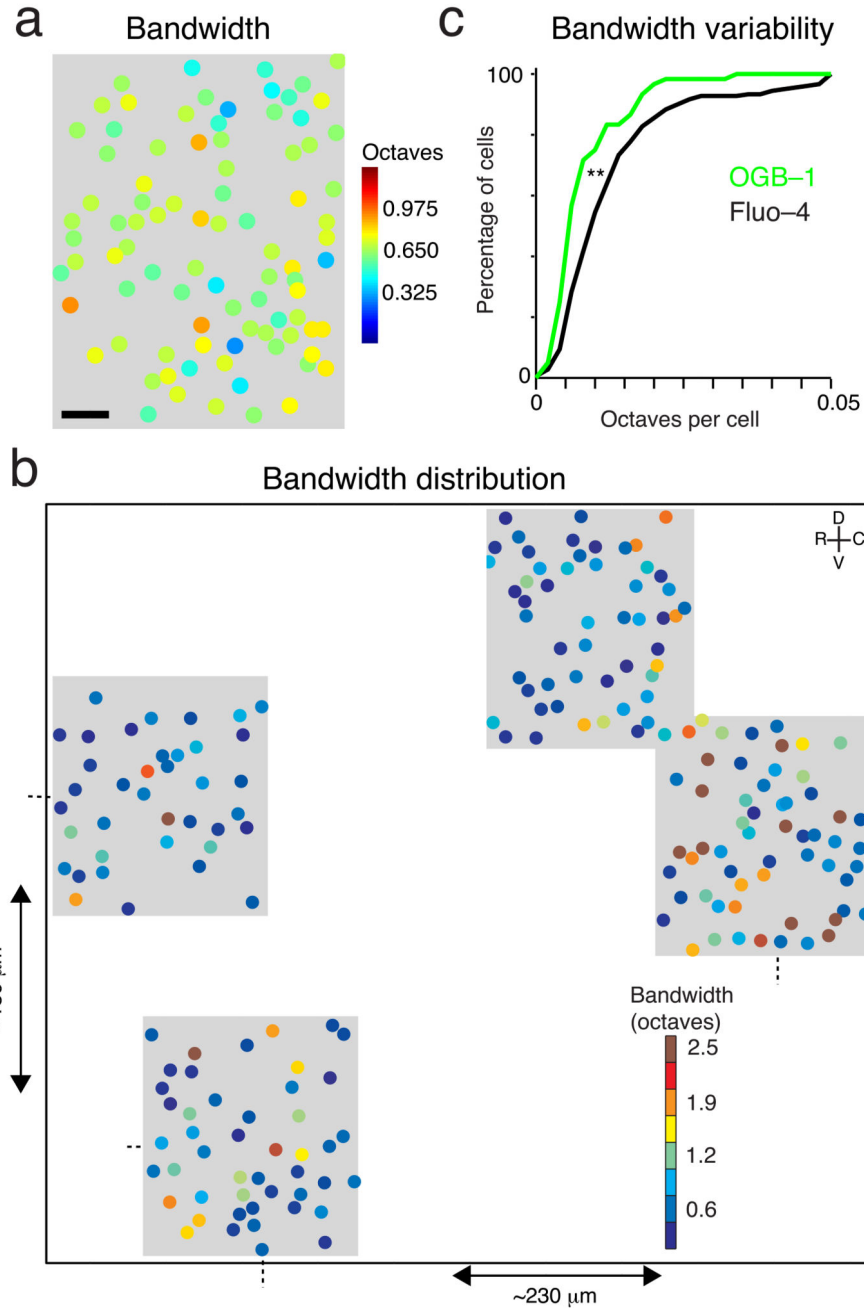


Figure 5. High local variability in bandwidth

a: Color-coded plot of bandwidth variation in A1 for the leftmost field in **Fig. 3c** shows varied bandwidth in nearby cells. Scale bar = 20 μm. **b:** Large-scale reconstruction of bandwidths is shown for the area imaged for the example in **Fig. 4a**; this case shows similar heterogeneity of bandwidths as in **Fig. 5a**. **c:** Cumulative distribution of variability of bandwidth within imaging sites shows that variability was lower for cells imaged with OGB-1 than with Fluo-4 (0.007 and 0.01, $P < 10^{-4}$, ‘**’, $n = 15$ animals with OGB-1 and

24 animals with Fluo-4). Variability was measured as the standard deviation of bandwidths normalized by the number of cells in the field of view.

Author Manuscript

Author Manuscript

Author Manuscript

Author Manuscript

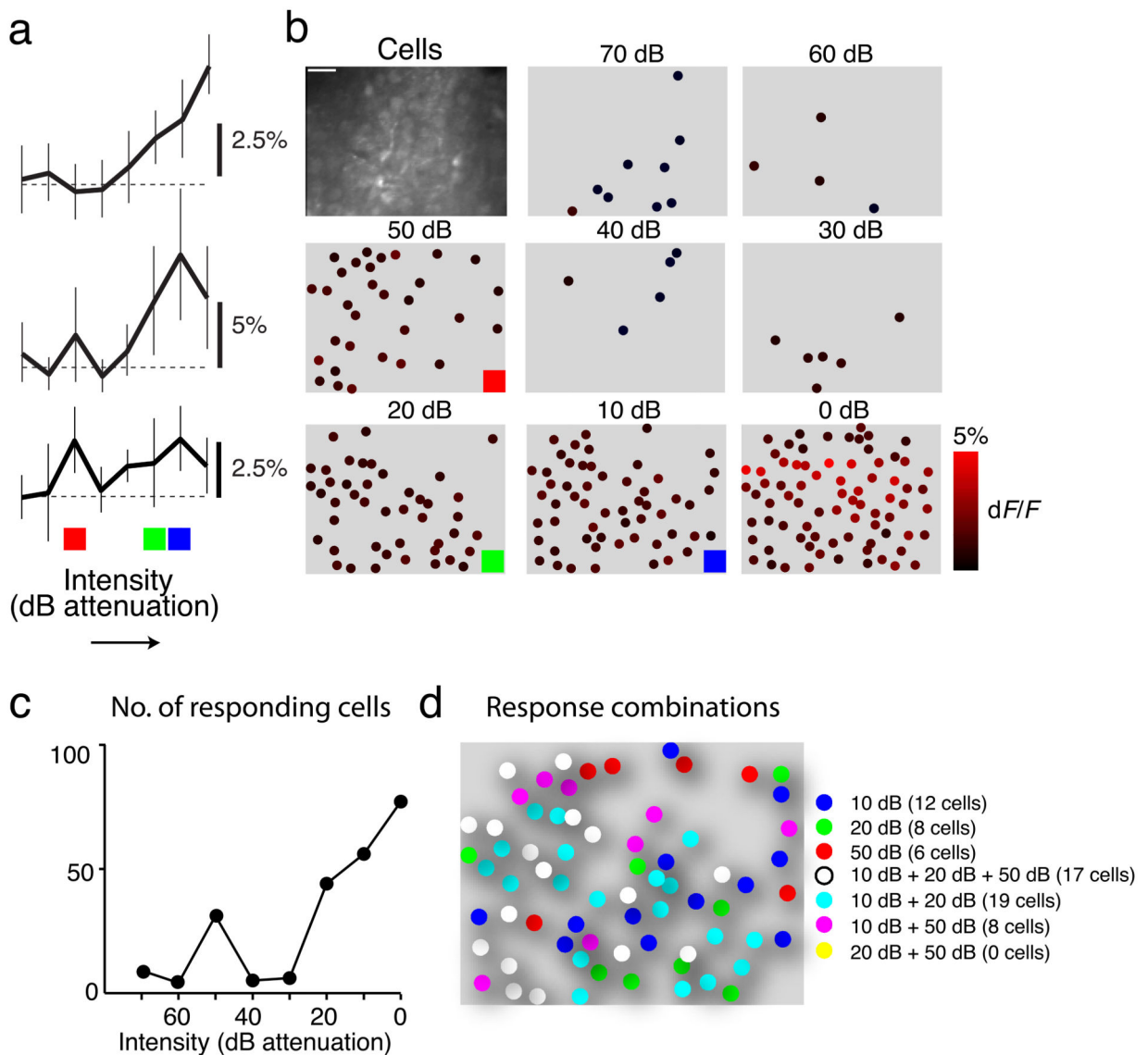


Figure 6. Intensity tuning and local heterogeneity in noise responses

a: Traces show maximum mean fluorescence changes to SAM noise stimuli with increasing intensity (decreasing attenuation) in 3 cells. Cells can show monotonic (top) and nonmonotonic (middle and bottom) intensity tuning curves. Nonmonotonic tuning curves were identified by a significant decrease in dF/F at higher intensities. Errorbars show 95% confidence intervals. **b:** Plotted are cells in one imaging site (top left) that responded to noise at a particular intensity ('activation plot'). Intensity levels are given as dB attenuation. Brightness of circles indicates response strength (maximum mean dF/F) (colorbar, right). Note that different populations of cells responded at each intensity. Scale bar shows $20\ \mu\text{m}$. **c:** Shown is the number of cells activated at various intensities indicating a nonmonotonic population representation of sound intensity. **d:** Shown is the superposition of 3 of the activation plots in **b** identified by colored squares. Colors of cells depict which combination of the 3 (red, green and blue squares) intensities a cell responded (example *white* – all 3

intensities, *cyan* – green and blue intensities). Note that the response properties of nearby cells are heterogeneous.

Author Manuscript

Author Manuscript

Author Manuscript

Author Manuscript

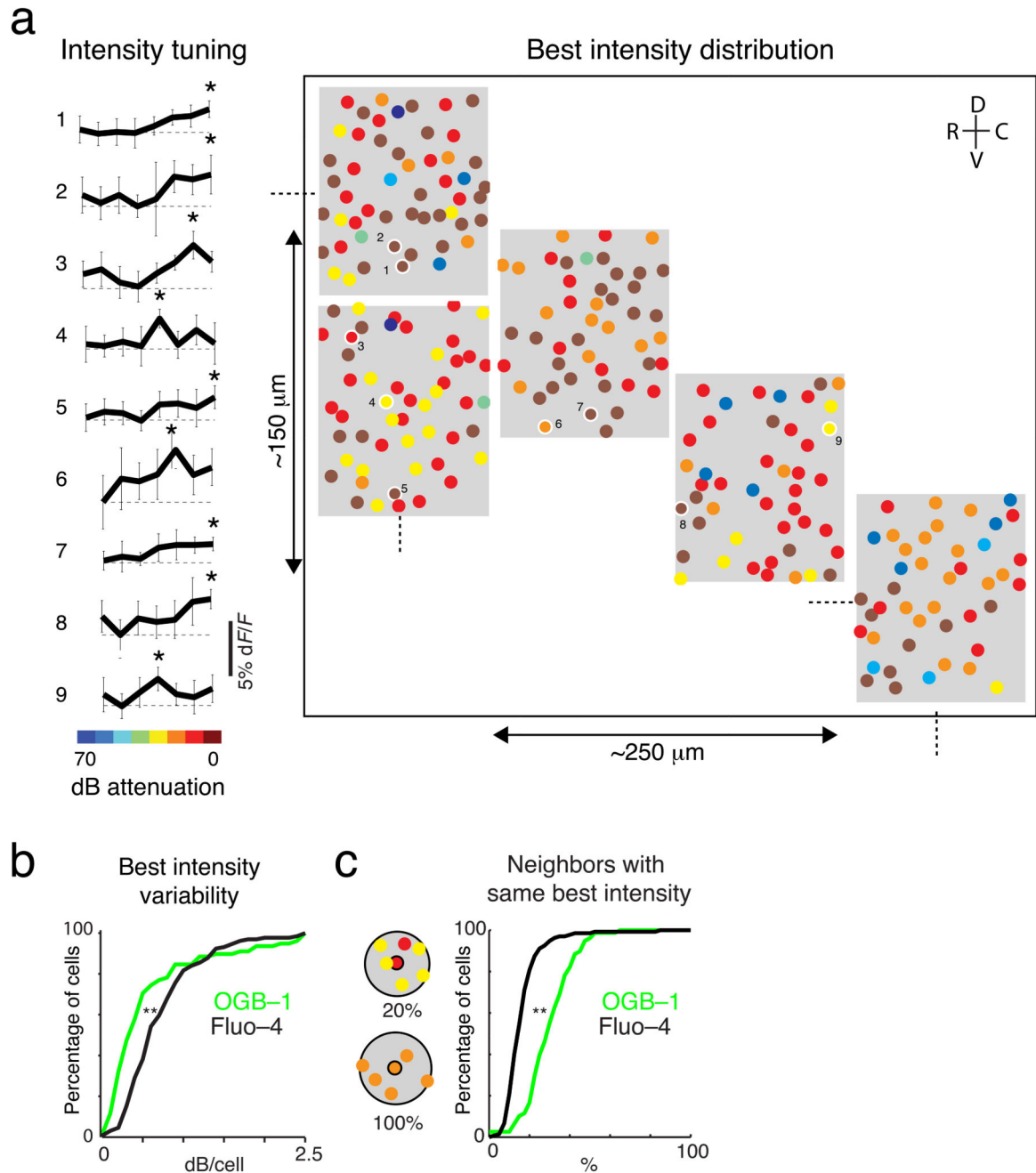


Figure 7. Figure 7. Lack of organized intensity maps

a: Reconstruction of 5 imaging sites in ACX (boxes) of one animal depicting the best intensities of cells in response to SAM broadband noise. The colors of the circles indicate the preferred intensity (colorbar). There is no clear pattern of organization of best intensities. Traces on left show intensity functions of 9 cells indicated in the reconstruction. '*' denotes the best intensity. Note that some cells showed monotonic while others showed nonmonotonic intensity functions. **b:** Cumulative distribution of best intensity variability within an imaging site. Variability was lower for cells imaged with OGB-1 than those

imaged with Fluo-4 ($P < 10^{-5}$, ranksum, ‘***’, $n = 15$ animals with OGB-1 and 24 animals with Fluo-4). Values were normalized by the number of cells in the field of view. **c**: Cumulative population distribution of average percentage of cells in 5 neighboring cells in a field of view that had the same preferred intensity as the central cell. OGB-1 showed more ($P < 10^{-10}$) percentage of cells on average (30%) had same preferred intensity as the central cell than with Fluo-4 (15%). Cartoon on the left shows how the local percentages were computed (same population as in **b**).

Author Manuscript

Author Manuscript

Author Manuscript

Author Manuscript

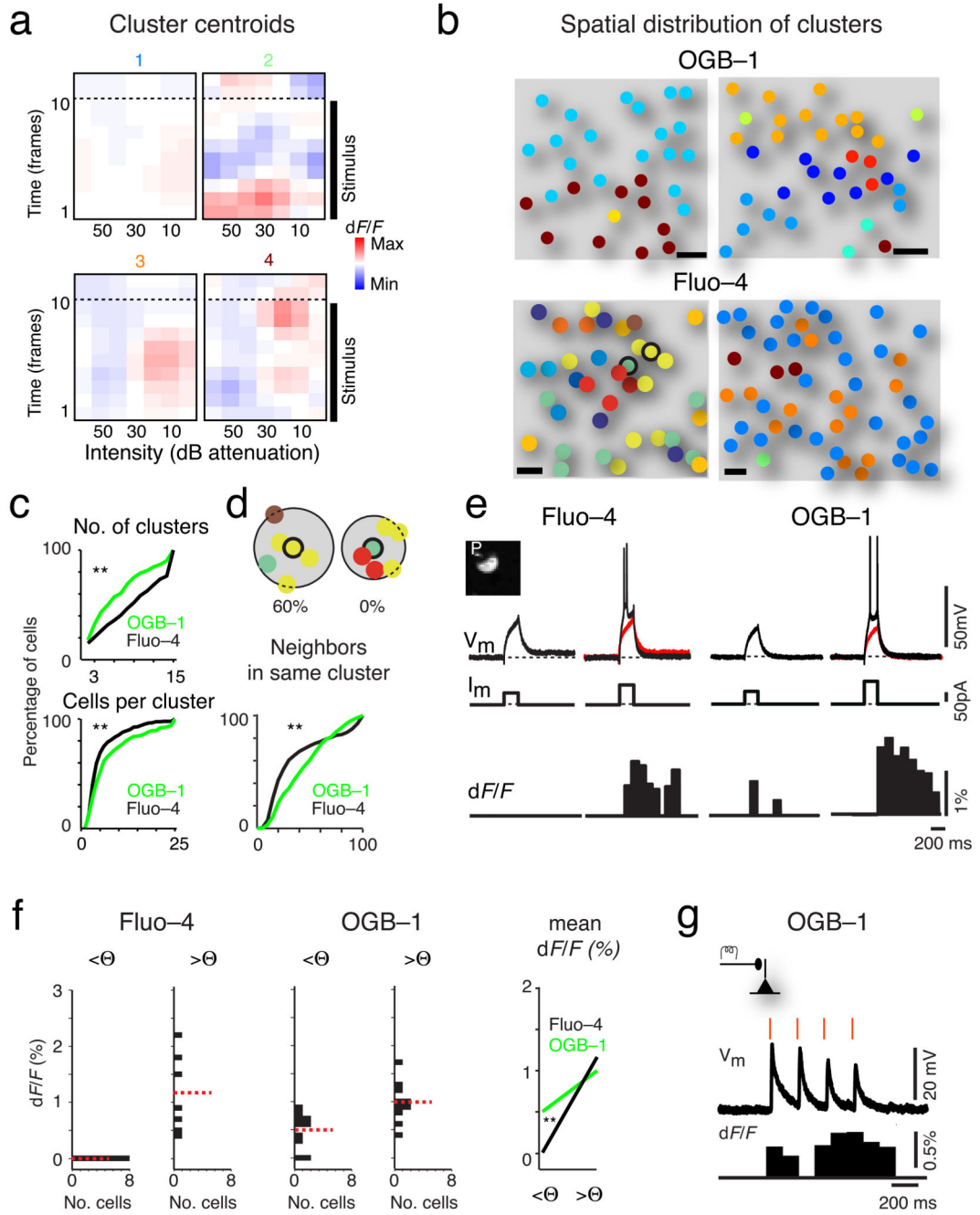


Figure 8. ACX cells receive shared inputs but respond differentially

a: Mean response characteristics (centroids) of 4 clusters formed in **b** (lower right image, label color indicates cluster). **b:** Examples of cluster formation to SAM tone or noise sets with OGB-1 (upper) and Fluo-4 (lower). Cells in each cluster have same color. The within to inter cluster distance ratios indicating degree of cluster separation are 0.358, 0.988 for OGB-1 and 0.871, 0.590 for Fluo-4. **c:** Cumulative distributions of cluster number and size ($P < 0.05$ ******), $n = 15$ animals with OGB-1, $n = 24$ with Fluo-4). **d:** Fraction of neighbors in same cluster (numbers of cells within the same cluster from the 5 nearest neighbors).

Analysis illustrated (top) for 2 cells in **b** (bottom left, black circles). Cumulative distributions (bottom) are different (KS-test, $P < 10^{-8}$, same animals as **c**). **e**: In vitro current-clamp recordings and 2-photon imaging of 2 cells filled with Fluo-4 and OGB-1 respectively. Inset shows image of one recorded cell ('P': patch pipette). Traces show membrane voltage (V_m , upper), current (I_m , middle), and significant (outside 95% confidence interval) mean dF/F (10 repeats, lower). Red traces show the respective subthreshold depolarization (left) in suprathreshold traces. **f**: Distributions of in vitro dF/F for the 2 categories for each cell (OGB-1 $n = 10$, Fluo-4 $n = 7$ cells): highest subthreshold depolarization tested and spiking. Means indicated by red lines. Peak depolarization (22 ± 5 mV and 23 ± 7 mV respectively, $P = 0.65$) and membrane charging times for OGB-1 and Fluo-4 were similar ($P > 0.5$). **g**: Traces show V_m (top) and mean dF/F (bottom, 20 repeats) during electrical stimulation (4 pulses, red lines) of horizontal inputs (cartoon).